Tailoring of metal cluster-like materials for the molecular oxygen reduction reaction*

Nicolas Alonso-Vante

Laboratory of Electrocatalysis, UMR-CNRS 6503, University of Poitiers, 40 Avenue du Recteur Pineau, 86022 Poitiers, France

Abstract: Research of nanometer scale range catalysts based on cluster-like mono-, bi-metallic, and chalcogenides for oxygen reduction reaction (ORR) as cathodes, a major challenge for polymer electrolyte membrane fuel cells (PEMFCs) nowadays, for facilitating efficient electron transfer using the carbonyl chemical route is reviewed. A strategy aimed at reducing the amount of expensive catalyst materials, giving the accessibility of non-noble materials and taking into account the activity and selectivity of cathodes for the ORR is devised as well.

Keywords: electrocatalyst; multi-electron charge transfer; acid solution; ruthenium; platinum; nanoalloys; nanomaterials.

INTRODUCTION

Investigation of multi-electron charge-transfer mechanisms, such as the oxygen reduction reaction (ORR), is of relevance for both fundamental electrochemistry and materials science. This is the process at the cathode in low-temperature polymer electrolyte membrane fuel cells (PEMFCs). This system possesses high energy conversion efficiency, operates at relatively low temperature, and furnishes environmental benefits. However, in order for the system to become commercially viable, it is necessary to address at least two major barriers, i.e., (i) cost and (ii) performance durability. The cost barrier is the key to the success of high-power fuel cell systems for the automotive industry and stationary power applications. The durability barrier, on the other hand, is relevant to all fuel cell systems, including those for portable applications.

Significant progress has been achieved, for fuel cell system cathodes, in the search for nanometer scale range catalysts based on cluster-like mono-, bi-metallic, and chalcogenides. Conversely, whatever the economic issue, the tailoring per se of efficient and selective cathode catalysts in the nanoscale domain [1] is interesting and still challenging for the ORR process. Our understanding of such a process is increasing thanks to the computational tools developed nowadays, see, e.g., [2,3]. Pt-based cathode catalysts have an additional disadvantage of being intolerant to small organic molecules (e.g., methanol), which leads to the performance and efficiency loss due to the formation of a mixed potential [4]. Unlike Pt, alternative ORR catalysts promise to be either fully or partially methanol-tolerant, thus providing additional benefits for cells using such an organic molecule as a fuel.

As noted above, the tailoring of materials for a defined purpose is essential. In this sense, the carbonyl chemical synthesis route proved to be a good alternative for electrocatalyst design, see [1] and
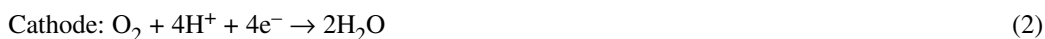
---

references therein. The materials issued from this approach have also been applied for catalysis [5–9]. This chemical route represents a way among others that use, e.g., high-throughput screening [10,11] and chemical deposition [12–17].

A family of novel catalysts such as nanoalloys and chalcogenide based on Pt, Ru, and Co has been generated via carbonyl molecular precursors (bottom-up approach). These catalysts are either the state of the art, or in the state of development in our group. They will be mainly discussed in terms of the ORR in acid medium.

FUEL CELL REACTIONS

The overall electrochemical reactions taking place in a PEMFC system are

Anode: $2H_2 \rightarrow 4H^+ + 4e^-$ (1)

Cathode: $O_2 + 4H^+ + 4e^- \rightarrow 2H_2O$ (2)

Net reaction: $2H_2 + O_2 \rightarrow 2H_2O$ (3)

The underlying mechanism of processes 1 and 2 depends both on the electrolyte nature and the catalyst (single crystals or faceting nanoparticles). Since this work is devoted to ORR, it is worth mentioning that process 1 proceeds very fast and with nearly no activation loss when the catalyst is Pt [18]. Under similar conditions, however, process 2 is two orders of magnitude slower than process 1, and therefore it represents the main activation loss of a PEMFC, see scheme in Fig. 1.
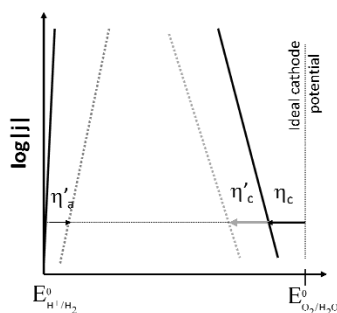

Fig. 1 Hydrogen oxidation (anode) and oxygen reduction (cathode) reactions in the activation region (full lines). Additional activation losses (dashed lines).

Activation region

The current–potential characteristic of these anodic and cathodic electrochemical reactions (e.g., onto Pt electrodes), can be, respectively, represented schematically by the straight lines, Fig. 1, according to simple kinetics given by the Butler–Volmer relation [19]

$$j = j_0 \exp\left(\alpha \frac{nF\eta_a}{RT}\right); \quad j = j_0 \exp\left[-(1-\alpha)\frac{nF\eta_c}{RT}\right]$$ (4)

with α being the transfer coefficient and j_0 the exchange current density. The equation can be rewritten as: $\eta = a + b \log j$; with $a = (-2.303RT/\alpha nF) \log j_0$, and $b = 2.303RT/\alpha nF$ (the Tafel slope). As it is well known, the best catalyst for the hydrogen oxidation eq. 1 is Pt, since this reaction proceeds at a negligible overpotential, η_a. However, at the cathode side there is an *intrinsic* loss, i.e., a substantial overpotential, η_c, of ca. 300 mV [20]. This process remains the most difficult multi-electron charge-transfer reaction even for the "best" known catalyst, Pt.

As schematically shown in Fig. 1, both processes are further affected by the nature of the fuel, i.e., other than hydrogen at the anode side inducing a "η'_a" and, by the performance of the membrane (e.g., Nafion®) which does not avoid the cross-over effect (when the fuel is methanol), at the cathode side [21], thus a "η'_c".

The diminution of the overpotential, η_c, at the cathode is a challenge, since on the one hand, it is necessary to develop a very active catalyst, and on the other hand, an augmented tolerance and/or selectivity either toward hydrogen ($\eta'_a \sim 0$) or oxygen ($\eta'_c \sim 0$) are desired.

DO WE HAVE THE CHEMICAL PRECURSOR TO TAILOR NANOCATALYST?

Nanodivided electrocatalyst can be generated under mild conditions taking advantage of chemical precursors [1,22]. These latter are generally transition-metal complexes, whose base structure may contain the ingredient, the so-called metallic cluster. One illustrative example of such chemical precursors can be given by the complex developed by Adams et al. [23]. They reported that $Pt_2Ru_4(CO)_{18}$, Fig. 2, was obtained by reacting $Ru(CO)_5$ and $Pt(cyclooctadiene)_2$.
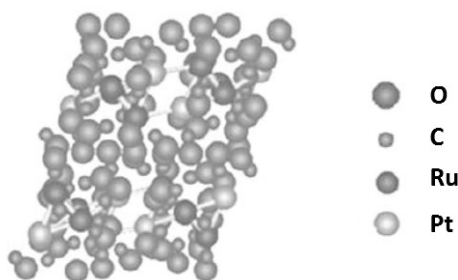

Fig. 2 Unit cell of $Pt_2Ru_4(CO)_{18}$ cluster compound generated from X-ray data reported in [23].

Later, the evolution of this molecular cluster as well as the carbide $PtRu_5C(CO)_{16}$ to obtain a bimetallic catalyst (Pt–Ru) supported onto carbon substrate was reported by the group of Nuzzo et al. [24,25]. These authors demonstrated that mixed Pt–Ru nanoparticles, with an extremely narrow size distribution (particle size 1.4 nm), were obtained. The Pt–Pt, Pt–Ru, and Ru–Ru coordination distances in the precursor (2.66, 2.64, and 2.84 Å) [23] changed to 2.73, 2.70, and 2.66 Å, respectively, on the mixed-metal nanoparticles supported onto carbon black, with an enhanced crystalline disorder, as revealed by X-ray absorption fine structure (XAFS) spectroscopy. This example, using a controlled pyrolysis onto a designed molecular cluster, succeeds the process developed in our group using the non-aqueous solvents route [1] and gives account of the dynamics of the molecular compound to the final material during the annealing process. In spite of this, within the aim of understanding the growth of metal cluster in solution, one starts from a metal complex precursor, such as $[M_y(CO)_x]$. This process can perhaps be best illustrated by the set of reactions schematized in Fig. 3, which is a very simplistic view of the rather complex chemical interplay of the nanocrystal growth.
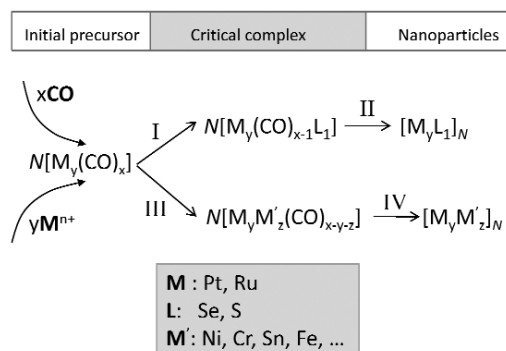
Fig. 3 The reaction scheme illustrates the fundamental steps to generate nanoparticles via the carbonyl chemical route in organic solvents. This route generates an intermediate precursor, the so-called critical complex $[M_y(CO)_{x-1}L_1]$ or $[M_yM_z'(CO)_{x-y-z}]$. The $N[M_y(CO)_x]$ species represents the number of initial molecular precursor complex either from a commercial source, e.g., $[Ru_3(CO)_{12}]$ or from chemical synthesis, e.g., $[Pt_3(CO)_6]_n^{2-}$. The kinetics of paths I and III, to form the critical complex, will depend on the nature of the additives, L (e.g., Se), into the reaction vessel, and M' of the salt containing the metallic cations, respectively. The solvent plays a role as a ligand (L) in the absence of a chalcogen (see text).

Ruthenium- and platinum-based materials

Ruthenium cluster-like materials
In the solution synthesis route, the important issue, although difficult to follow up in situ, is the generation of the critical complex. In some cases, as the example illustrated above, these species can be generated separately [23]. Moreover, it is interesting to recognize that the final catalytic nanoparticles are determined by the nature of these in situ generated critical complexes, in the solution, and further by the kinetics of paths II and IV. In the development of Ru chalcogenide materials and related materials, in mild conditions, for ORR electrocatalysis, it is very popular to consider the tris-ruthenium dodeca-carbonyl $Ru_3(CO)_{12}$ as the initial chemical precursor. A "simple" pyrolysis at the boiling point of the organic solvent (e.g., xylene) of this molecular complex leads to nanoparticles of ruthenium, Ru_x [26]. However, the insight into the pyrolysis of $Ru_3(CO)_{12}$ in xylene, according to the scheme of Fig. 3, was obtained by Fourier transform infrared (FTIR) follow-up during the synthesis. The generated critical complexes were further identified by ^{13}C-NMR [22,27]. FTIR is a very popular technique and delivers the necessary preliminary data, as illustrated in Fig. 4. Indeed, without the addition of any other element (e.g., Se), the pyrolysis reaction kinetics is determined by the temperature of the solvent, the release of the CO ligands during pyrolysis, and the coordination ability of the solvent molecules (L = xylene) during the synthesis. Figure 4a shows the FTIR at a reaction time of 70 min (upper curve). The addition of elemental Se, which dissolves in the organic solvent, influences the reaction kinetics (see Fig. 4b upper curve), and therefore the nature of the critical complex. This can be visualized by comparing the spectrum of the initial precursor. In the depicted energy interval in the same solvent and time of reaction, other vibration modes appear. The difference is clear at the end of the synthesis; see curves at the bottom of Figs. 4a and 4b. In the case (a) the band positions, e.g., at 2064, 2049, and 2007 cm^{-1}, as well as 2079, 2034, 2027, and 2012 cm^{-1}, have been attributed to $[Ru_6C(CO)_{14}–(L)]$, where L = xylene = $(CH_3)_2C_6H_4$ [24,27]. This so-called, critical cluster complex is stable in this medium [28,29], and the yield of nanoparticles of Ru_x via this route is very low (ca. ~20 %). Moreover, after 70 min reaction time, path I is kinetically favored to generate the nuclei of the critical complex in the first minutes in xylene in the presence of Se, see Fig. 4b. We observe bands at 2060 and 2031 cm^{-1}, apparently belonging to the parent complex. In spite of this, the results obtained via the ^{13}C-NMR technique seem to indicate the presence of a seleno-ruthenium-carbonyl complex. This compound was identified as
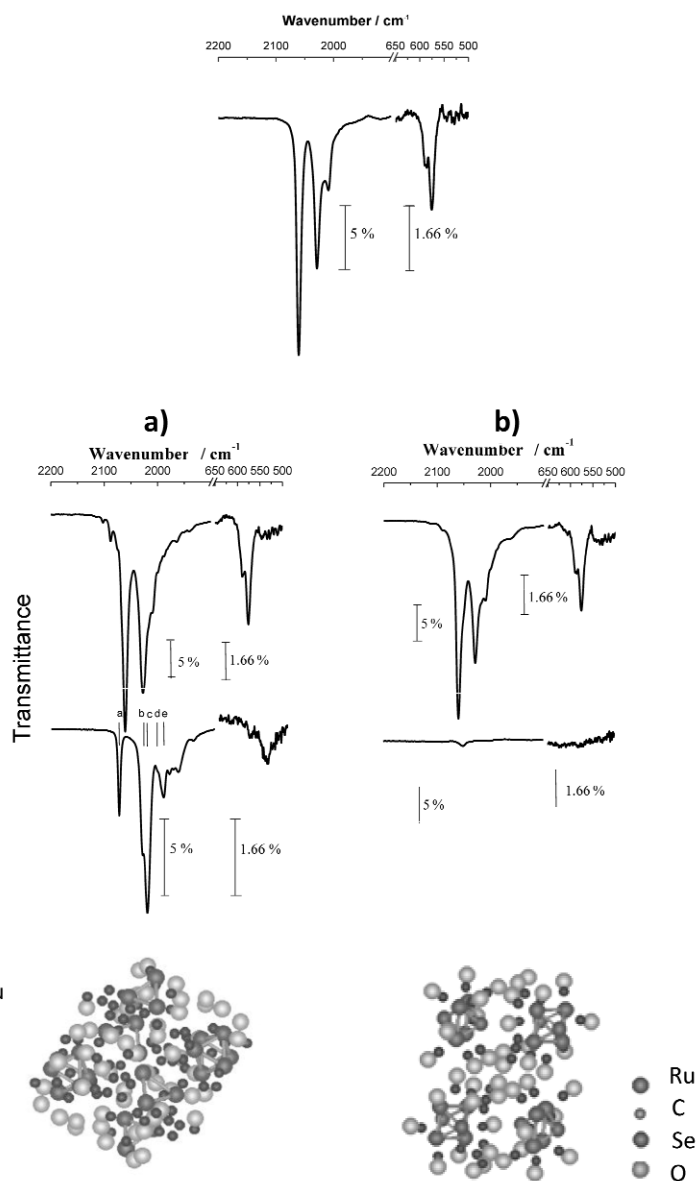
Fig. 4 FTIR spectra reaction evolution of $Ru_3(CO)_{12}$, in xylene, (a) without Se; (b) with Se. The bars a, b, c, d, and e indicate the position of the peaks at: 2074, 2032, 2023, 2005, and 1994 cm^{-1}, respectively. The upper panel shows the FTIR spectrum of the parent transition-metal complex $[Ru_3(CO)_{12}]$. The panels, at the bottom, show the unit cells of the transition-metal clusters compounds, left: $[Ru_6C(CO)_{14}-((CH_3)_2C_6H_4)]$ [27]; and, right: $[Ru_4Se_2(CO)_{11}]$ [30] generated in the processes a and b.

$Ru_4Se_2(CO)_{11}$ [22,26,27]. This latter is not stable at the synthesis conditions, and its pyrolysis (cf. curve b, bottom) leads to Ru_xSe_y. The use of Se leads to a yield of ≥90 %. The separation of this critical complex was done, and its structural dynamics were followed up using wide-angle X-ray spectroscopy (WAXS) [30]. This study furnished a clear evidence of the process via the chemical route. This finding is interesting; first, it indirectly confirms the formation of a cluster-like material; and second, it is the

real chemical precursor that incorporates or coordinates into the structure, the ligand Se leading in the end to Ru_xSe_y (where $x \approx 2$ and $y \approx 1$) [22,26].

In an attempt to minimize the amount of Ru in Ru_xSe_y nanoparticles, we focused on partially replacing Ru by Fe [31], following the strategy devised in Fig. 3, i.e., L was Se (first added) and subsequently $Fe(CO)_5$. The X-ray diffraction (XRD) pattern of Ru–Fe–Se (results not shown here) indicates that the main broad Ru peak is shifted toward higher angles, evidencing that an alloy formation between Ru and Fe takes place [32]. It is clear that the obtained nanoparticles are a result of a complex interplay between the $Ru_4Se_2(CO)_{11}$, previously formed, and the decomposition of the iron pentacarbonyl. We do not have the experimental evidence of such a critical complex formation (Ru–Fe–Se–CO). Nevertheless, due to the important dilution effect of the Ru cluster by 50 at. % of iron at the nanodivided form of Ru_xSe_y, and the unchanged electrocatalytic activity for the ORR, the catalyst could be fashioned by a core-shell, i.e., Fe–Ru_xSe_y structure [32]. Figure 5 supports this expectation, though it shows a simple cyclic voltammetry evolution of this novel xylene-generated catalyst in 0.5 M H_2SO_4.

As observed, the current–potential curves indicate the surface reaction response evolution of the Ru_1Fe_1Se nanoparticles, as a function of the number of cycling in acid medium. The waves, centered at the iron oxidation/reduction potential (0.7 V/RHE) disappear after a certain number of cycles. The wave shows, however, that on the as-prepared nanocatalyst, Fe is still present at the nanoparticles' surfaces. This stabilized electrochemical response accounts for the response of a surface-like Ru–chalcogenide [26,33].
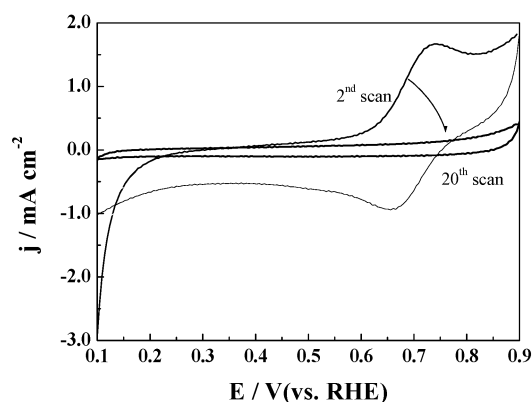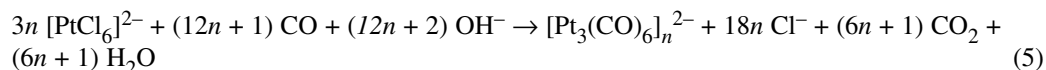

Fig. 5 Current–potential characteristics of xylene non-carbon-supported synthesized nanoparticles with 50 at. % substitution of Ru by iron: Ru_1Fe_1Se, in N_2-saturated 0.5 M H_2SO_4 at 100 mV s^{-1}. For the sake of clarity, only the 2nd and 20th cycles are shown.

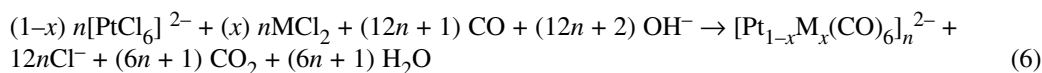Platinum cluster-like materials

The generation of Pt nanoparticles takes its origin in the use of Pt carbonyl complex: $[Pt_3(CO)_6]_{\sim n}^{2-}$, and it is generated from $Na_2PtCl_6 \cdot 6H_2O$, after eq. 5:

$$3n\ [PtCl_6]^{2-} + (12n + 1)\ CO + (12n + 2)\ OH^- \rightarrow [Pt_3(CO)_6]_n^{2-} + 18n\ Cl^- + (6n + 1)\ CO_2 +$$
$$(6n + 1)\ H_2O \qquad (5)$$

This $[Pt_3(CO)_6]_n^{2-}$ was first reported by Longoni and Chini in the 1970s [34] and serves as the building block for $N[M_y(CO)_x]$ to synthesize bi-metallic nanocatalysts. The reactivity of this initial precursor, $[Pt_3(CO)_6]_n^{2-}$ with $n = 5$, is an advantage to preparing bi-metallic nanocatalyst when L_1 is added in the form of metallic salts containing Sn, Ni, Cr, or Co. Up to now, the extent to which the metal atoms are involved in the intermediate complex formation with Pt is still not clear, i.e., the critical complex generation. The feasibility, according to the scheme in Fig. 3, is that the critical complex must possess

a stoichiometry like [Pt$_y$M'$_z$(CO)$_{x-y-z}$]. The experimental evidences in this respect are scarce up to now. However, following the same principle as discussed for the chalcogenide materials synthesis (see above), the results, regarding the Pt-based materials, strongly support this expectation. In this sense, Pt$_y$–M'$_z$ alloys (M' = Ni, Cr, Fe, Co) were generated [35–38] following the general chemical reaction 6

$$(1–x) \; n[\text{PtCl}_6]^{2-} + (x) \; n\text{MCl}_2 + (12n + 1) \; \text{CO} + (12n + 2) \; \text{OH}^- \rightarrow [\text{Pt}_{1–x}\text{M}_x(\text{CO})_6]_n^{2-} +$$
$$12n\text{Cl}^- + (6n + 1) \; \text{CO}_2 + (6n + 1) \; \text{H}_2\text{O} \tag{6}$$

As depicted by this general equation, firstly, it shows that the presence of the critical complex is a necessary step (see path III, Fig. 3), and secondly, that solid nanoparticle solutions of the type Pt$_{1–x}$M$_x$, toward the nanoalloy catalysts on the basis of Pt, are also feasible (path IV). Figure 6 shows the FTIR spectra corresponding to the CO vibration modes in the energy interval between 1750 and 2150 cm^{-1}. As shown by eq. 5, the nuclei of [Pt$_3$(CO)$_6$]$_n^{2-}$ are already synthesized after an induction time of ca. 2 h (result not shown here) in a CO-saturated methanol solution containing a proportion of NaOH:CH$_3$COONa (4:4), so that a ratio CH$_3$COONa/Pt = 6 produces a Pt cluster with n = 5, i.e., [Pt$_3$(CO)$_6$]$_5^{2-}$, see curve A in Fig. 6. It is worth mentioning that the solvent containing methanol produces, in the energy interval shown in Fig. 6, a small peak centered at 2045 cm^{-1}. Therefore, the broad bands centered at 2053 and 1880 cm^{-1} correspond to the CO vibration mode of the Pt–CO complex. This result is in agreement with results reported some time ago by Longoni and Chini [34]. The Pt cluster carbonyl complex remains stable in CO-saturated atmosphere. Now, following the scheme in Fig. 3 and eq. 6, a similar evolution of the reaction is obtained in the presence of Co cations. Small differences, regarding the FTIR spectrum (see curve B) are observed, which could be attributed to [Pt$_{1–x}$Co$_x$(CO)$_6$]$_n^{2-}$. Again, this intermediate or critical complex is stable in CO atmosphere. The completion of the reaction to obtain the nanoparticles (step IV) is simply done in mild conditions in the presence of a controlled amount of oxygen and the addition of a carbon substrate as catalyst support. A further treatment can be necessary, such as washing, thereafter annealing in hydrogen atmosphere to eliminate trace amount of oxides.
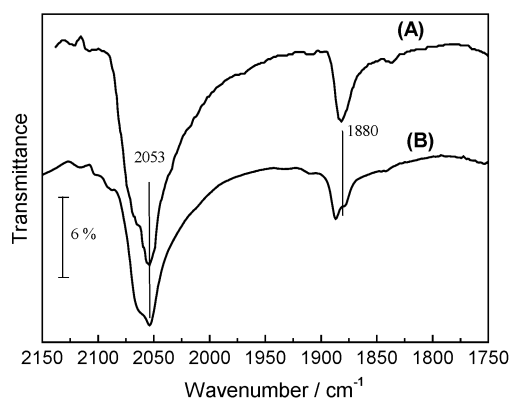

Fig. 6 FTIR spectra reaction evolution of (A) [PtCl$_6$]$^{2-}$; and (B) [PtCl$_6$]$^{2-}$ and CoCl$_2$, after 20 h reaction in CO-saturated methanol solution.

In order to illustrate the dispersion of such materials obtained by this route, Fig. 7 depicts a series of XRD spectra recorded on a series of Pt–Co alloys in the angle interval of 2θ from 30° to 60°. From pure Pt nanoparticles, the alloy formation is clearly observed by the shift of the main Bragg diffraction peak (111) to higher angles, further, the full width at half maximum (FWHM) of the peaks is relatively large due to the particle size and crystalline disorder of the nanomaterials. Then, as compared to Pt, the Pt–Co diffraction curves, within the experimental error, do not show the presence of another
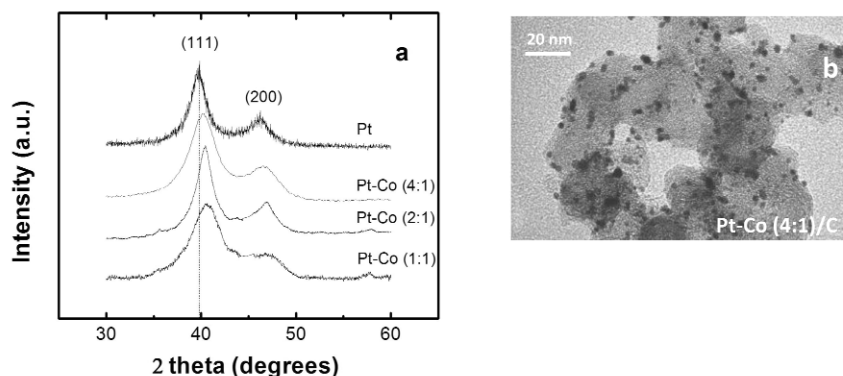
Fig. 7 (a) A series of X-ray diffractograms of Pt, and bimetallic Pt–Co catalysts developed via the carbonyl chemical route; (b) TEM image of Pt–Co(4:1)/C.

phase. The dispersion of the particles is appreciated in a typical transmission electron microscopy (TEM) picture shown in Fig. 7b, which corresponds to the sample 20 wt % Pt–Co(4:1)/C. The particle size analysis of Fig. 7b revealed a size distribution of 2.40 ± 1.06 nm. A similar behavior was found for other alloys such as Pt–Ni.

WHAT IS THE IMPORTANCE OF THE LIGAND EFFECT IN THE NANOCATALYST?

The ligand effect (or electronic effect) is a phenomenon that takes place in surface reactivity. Such an effect was recently discussed on the basis of extensive density functional theory calculations in order to rationalize the reactivity in heterogeneous catalysis and electrochemistry [39]. Most metallic nano-catalysts are prone to surface oxidation processes in air atmosphere. At the electrochemical interface, water discharge may take place at potentials lower than the thermodynamic potential of the ORR. Since for Pt material this oxidation takes place at 1.188 V/NHE [20], this implies that Pt_xO_y species are possible to be formed at the open-circuit potential or at around 1 V/RHE. A striking example of surface evolution toward the formation of oxide-like species either in air or in contact with water is Ru, since its surface energy is higher than that of Pt [40].

At the nanodivided scale, the ignition effect with oxygen from air is even enhanced. The outer-most surface of Ru nanoparticles is thus covered by clusters of Ru_xO_y species [41]. One way to diminish this oxidation process is to perform the Ru surface coordination with a ligand able to accept charges such as Se, thus rendering the Ru surface atoms less labile to further coordinate with oxygen to form oxides. The experimental evidence of such a phenomenon was recently reported [42]. Indeed, solid-state ^{77}Se NMR measurements showed that Se (a semiconductor with $E_g = 1.8$ eV) becomes metallic when bound to Ru, as indicated by the large Knight shift. The X-ray photoelectron spectroscopy (XPS) line shape also confirmed that the main peak of Se $3d_{5/2}$ is shifted toward lower binding energy (BE), suggesting that the BE shift refers to the Ru → Se charge transfer [42]. This ligand or electronic effect is the explanation to the observed chemical stability studied on Ru_xSe_y in comparison with Ru_x cluster-like materials by the WAXS technique [41], and recently further confirmed by in situ FTIR, using the adsorbed CO molecule as probe [43].

Further, the role of the ligand effect on Pt–Ru catalyst has been investigated via electrochemical nuclear magnetic resonance (EC-NMR) spectroscopy, which has emerged since 1990 as one useful probe to investigate the surface electronic properties of catalyst nanoparticles [44,45]. As, for example, in the Pt–Ru system, it is known that Ru improves the tolerance to CO on Pt nanoparticles in Pt–Ru alloys. The mechanism of promotion induced by Ru has been discussed in terms of bifunctional mechanism [45–48] and ligand effect [39,45,46]. As discussed above, regarding the chemical stability of the

Ru$_x$Se$_y$, the ligand effect is also encountered on bimetallic and alloy surfaces. After the molecular dynamics simulations, it appears that Ru in the Pt surface weakens the bond of the molecule (CO) adsorbed on Pt [49]. Using the adsorbed CO, as a molecule probe EC-NMR revealed that this adsorbed species becomes metallic on Pt–Ru. The authors [44] explain this phenomenon by the mixing of CO molecular orbital with the conduction electron states of the transition metal. This is in line with the results obtained on Ru chalcogenide [42]. Like the effect of Se atoms onto Ru in Ru$_x$Se$_y$, the presence of Ru atoms alters the surface electronic properties of Pt. This electronic interplay of the alloying element M in Pt–M nanoalloy materials is of importance to understand the chemistry of the catalysts' surface. Other factors such as the increase of the d-band per atom as a function of the electron affinity of M, as well as the particle size effect have also been addressed by Mukerjee et al. using the extended X-ray absorption fine structure (EXAFS) technique [50,51].

TOLERANCE/SELECTIVITY TOWARD THE OXYGEN REDUCTION REACTION

Certainly, owing to the effect described above, Pt-based alloy catalysts such as Pt–Co, Pt–Ni, and Pt–Cr exhibit an enhanced catalytic activity for the ORR with respect to Pt alone as reported by various groups [52–54], whereas their selectivity toward ORR is not sustained when methanol is present in the electrolyte, or in a DMFC due to the cross-over effect. For this reason, electrocatalysts based on non-Pt materials with higher tolerance have been developed [1,22,55,56]. Nevertheless, among the Pt nanoalloys, Pt–Cr shows an enhanced tolerance to methanol during the ORR. Indeed, the carbonyl-generated Pt–Cr catalysts show higher ORR activity in the presence of 0.5 M CH$_3$OH in HClO$_4$ electrolyte solution, as compared with Pt–C alone in the same conditions, see Fig. 8a. Moreover, as compared to the ORR in pure HClO$_4$ solution (see curve 1), all the catalysts for the ORR showed an increase in overpotential under the same current density in the presence of methanol. At $j = –1$ mA cm^{-2}, for the ORR on pure Pt catalyst in methanol-containing solution, the overpotential increases by ca. 0.22 V and the onset potential decreases by ca. 0.30 V. The significant increase in overpotential of the ORR on pure Pt catalyst is due to the competitive reaction between oxygen reduction and methanol oxidation. By using the Pt–Cr alloy catalysts, there is also a decrease of the activity for the ORR in methanol-containing electrolyte. However, the potential loss on all these alloy catalysts is only ca. 0.06 V in comparison to that in pure HClO$_4$ acid solution. From the figure, it is very clear that the ORR activity on the Pt–Cr alloy catalysts in methanol-containing solution is much higher than that on pure Pt, indicating that the Pt–Cr alloys are more methanol-tolerant during the ORR than pure Pt catalyst (curves 2). Meanwhile, the current density of methanol oxidation in oxygen-saturated solution on the alloy catalysts at high potentials (above 0.85 V) is lower than on pure Pt catalyst, and it decreases with the increase of the Cr content. The result is that the Pt–Cr(1:1)/C catalyst appears to be the most active for the ORR in absence and in methanol-containing acid solutions.

On the other hand, Ru-based transition-metal chalcogenide catalysts are fully tolerant, as reported some time ago [57] to methanol, cf. curves 1 and 2 in Fig. 8b, although less active than Pt in the absence of methanol. The reason for this relative disadvantage is the presence of a mixed potential produced by the oxidation process of coordinated Se [55]. Therefore, it was interesting to show to what extent chalcogenide-modified Pt could compete with the Ru chalcogenide. The chemical synthesis, although different from the carbonyl route, to generate Pt$_x$S$_y$ [16] provided some clues as to its electrocatalytic performance. This comparison was performed in H$_2$SO$_4$ 0.5 M, as depicted in Fig. 8b. Indeed, the chalcogenide surface modification of Pt confers to this latter an enhanced tolerance to methanol, which lies at the level of the chalcogenide Ru$_x$Se$_y$. This phenomenon is direct evidence that Pt surface nanoparticle nature is modified by sulfur atoms, and its activity toward ORR is apparently less effective as compared to pure Pt nanoparticles (in the absence of methanol). The depolarization at $j = –1$ mA cm^{-2} effect, at the Pt$_x$S$_y$ (ca. 0.10–0.12 V) as compared to Pt (0.33 V) in 0.5 M H$_2$SO$_4$ + 0.5 M CH$_3$OH. Taking into consideration that electrocatalysis is mainly done by one chalcogenide-modified metal center, the present results add strength to the strategy of developing chalcogenide materials selective for
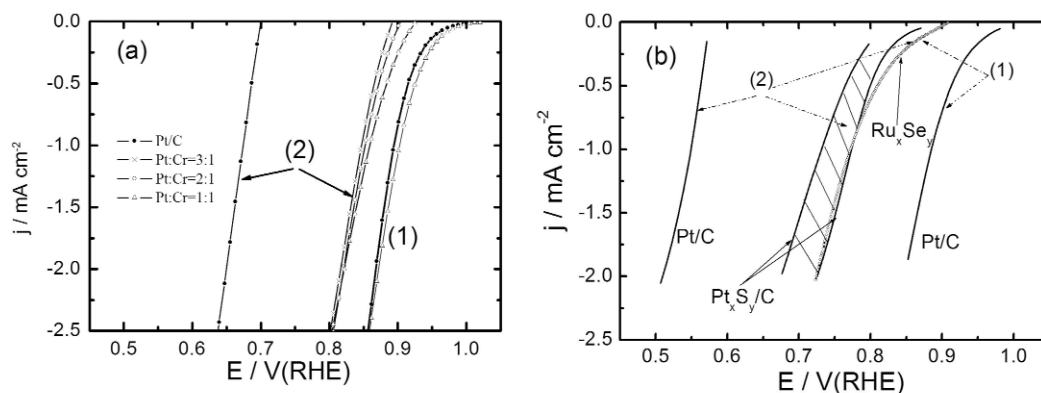
Fig. 8 ORR current–potential characteristics, in the activation region, in electrolytes saturated with pure oxygen on Pt- and Ru-based nanocatalysts in the absence (curves 1) and presence of 0.5 M CH_3OH (curves 2). (a) Linear scan voltammograms of the Pt/C catalyst and the carbon-supported nanosized Pt–Cr alloy catalysts in 0.5 M $HClO_4$ electrolyte, at the scan rate of 5 mV/s and the rotating speed of 2000 rpm. (b) Linear scans for Pt/C and Pt_xS_y/C, Ru_xSe_y in 0.5 M H_2SO_4 electrolyte at the scan rate of 5 mV/s and the rotating speed of 1600 rpm. The hashed lines for Pt_xS_y/C show the activity variation of various electrodes. The current–potential of chalcogenides remains unchanged in the absence or presence of methanol.

electrocatalysis. Pt_xSe_y reported recently by another group [58] arrives at a similar conclusion. It is, however, clear that the structural and electronic effects on such novel materials are the object of further investigation in our group.

SUMMARY AND OUTLOOK

The crucial step to generate cluster-like materials for the ORR electrocatalysis was discussed with regard to the initial chemical precursor. The carbonyl chemical route to prepare chalcogenides and nanoalloys showed interesting perspectives for tailoring novel materials. The importance of maintaining the electrocatalytic activity and/or to enhance the coordinative ability of active sites lies in the possibility of diluting this center in such a way as to improve the electronic effect. This task is double and needs more sophisticated techniques to prove this phenomenon. Another crucial step is the control of the dynamic of the cluster during pyrolysis, since this phenomenon will dictate the fate of the generated catalyst in the nanoscale range. We learned that chalcogen atoms organize preferentially on the surface of the core-formed agglomerated Ru atoms. Ru_xSe_y cluster-like materials are derived from pyrolysis of a heteronuclear transition-metal complex compound, and from static NMR Se showed a metallic behavior in Ru_xSe_y.

Interestingly, with Ru_xSe_y, a Se-rich surface is apparently preferred. It confers upon the material a remarkable stability against oxidation by virtue of coordinated Se atoms onto some surface, keeping some free sites for catalysis. The selectivity is also encountered and can be produced on low tolerant metal centers such as Pt, as demonstrated by alloying, and/or by coordinating with a chalcogen. Therefore, the tailoring via carbonyl route of synthesis reveals the importance of producing "positive" disorder and needs understanding though the nature of the active sites on the generated nanomaterials, such as Ru_xX_y, Ru_xFe_yX, and Pt_xX_y/C (X = Se, S) and Pt–M (Co, Ni, Cr, …) remains an active area of research.

ACKNOWLEDGMENT

REFERENCES

1. N. Alonso-Vante. *Fuel Cells* **6**, 182 (2006) and refs. therein.
2. J. Greeley, J. K. Nørskov. *Electrochim. Acta* **52**, 5829 (2007).
3. T. Jacob. *Fuel Cells* **6**, 159 (2006).
4. C. Y. Du, T. S. Zhao, W. W. Yang. *Electrochim. Acta* **52**, 5266 (2007).
5. R. Ugo, C. Dossi, R. Psaro. *J. Mol. Catal. A: Chem.* **107**, 13 (1996).
6. H. Li, B. He. *React. Funct. Polym.* **26**, 61 (1995).
7. M. Ichikawa, L. Rao, T. Kimura, A. Fukuoka. *J. Mol. Catal.* **62**, 15 (1990).
8. M. Ichikawa. *Polyhedron* **7**, 2351 (1988).
9. P. Maeki-Arvela, J. Hajek, T. Salmi, D. Yu Murzin. *Appl. Catal., A* **292**, 1 (2005).
10. E. S. Smotkin, J. Jiang, A. Nayar, R. Liu. *Appl. Surf. Sci.* **252**, 2573 (2006).
11. S. Guerin, B. E. Hayden, C. E. Lee, C. Mormiche, A. E. Russell. *J. Phys. Chem. B* **110**, 14355 (2006).
12. P. Trogadas, V. Ramani. *J. Power Sources* **174**, 159 (2007).
13. X. Li, H. R. Colon-Mercado, G. Wu, J.-W. Lee, B. N. Popov. *Electrochem. Solid-State Lett.* **10**, 201 (2007).
14. S. Shanmugam, A. Gedanken. *Small* **3**, 1189 (2007).
15. J. Tian, G. Sun, L. Jiang, S. Yan, Q. Mao, Q. Xin. *Electrochem. Commun.* **9**, 563 (2007).
16. Y. Gochi-Ponce, G. Alonso-Nunez, N. Alonso-Vante. *Electrochem. Commun.* **8**, 1487 (2006).
17. H. Yano, M. Kataoka, H. Yamashita, H. Uchida, M. Watanabe. *Langmuir* **23**, 6438 (2007).
18. M. S. Wilson, J. A. Valerio, S. Gottesfeld. *Electrochim. Acta* **40**, 355 (1995).
19. A. J. Bard, L. R. Faulkner. *Electrochemical Methods, Fundamental and Applications*, 2nd ed., John Wiley, New York (2001).
20. M. R. Tarasevich, A. Sadkowski, E. Yeager. In *Comprehensive Treatise in Electrochemistry*, J. O'M. Bockris, B. E. Conway, E. Yeager, S. U. M. Khan, R. E. White (Eds.), Chap. 6, Plenum, New York (1983).
21. A. Kuever, K. Potje-Kamloth. *Electrochim. Acta* **43**, 2527 (1998).
22. N. Alonso-Vante. "Novel nanostructured material based on transition metal compounds for electrocatalysis", in *Catalysis of Nanoparticles Surfaces*, A. Wieckowski, E. Savinova, C. Vayenas (Eds.), p. 931, Marcel Dekker, New York (2003).
23. R. D. Adams, G. Chen, W. Wu. *J. Cluster Sci.* **4**, 119 (1993).
24. C. W. Hills, M. S. Nashner, A. I. Frenkel, J. R. Shapley, R. G. Nuzzo. *Langmuir* **15**, 690 (1999).
25. M. S. Nashner, A. I. Frenkel, D. L. Adler, J. R. Shapley, R. G. Nuzzo. *J. Am. Chem. Soc.* **119**, 7760 (1997).
26. V. Le Rhun, N. Alonso-Vante. *J. New Mater. Electrochem. Syst.* **3**, 331 (2000).
27. V. Le Rhun. Ph.D. thesis, University of Poitiers (2001).
28. B. F. G. Johnson, R. D. Johnston, J. Lewis. *J. Chem. Soc.* 2865 (1968).
29. C. R. Eady, P. F. Jackson, B. F. C. Johnson, J. Lewis, M. C. Malatesta, M. McPartlin, W. J. H. Nelson. *J. Chem. Soc., Dalton Trans.* 383 (1980).
30. W. Vogel, P. Kaghazchi, T. Jacob, N. Alonso-Vante. *J. Phys. Chem. C* **111**, 3908 (2007).
31. C. Delacôte, C. M. Johnston, P. Zelenay, N. Alonso-Vante. 212th ECS Meeting, Chicago, Abs. nr. 229 (2007).
32. Unpublished data.
33. D. Cao, J. Inukai, A. Wieckowski, N. Alonso-Vante. *J. Electrochem. Soc.* **153**, A869 (2006).
34. G. Longoni, P. Chini. *J. Am. Chem. Soc.* **98**, 7225 (1976).
35. H. Yang, N. Alonso-Vante, C. Lamy, D. L. Akins. *J. Electrochem. Soc.* **152**, A704 (2005).
36. H. Yang, W. Vogel, C. Lamy, N. Alonso-Vante, *J. Phys. Chem. B* **108**, 11024 (2004).
37. H. Yang, N. Alonso-Vante, J.-M. Leger, C. Lamy. *J. Phys. Chem. B* **108**, 1938 (2004).
38. E. Favry. Ph.D. thesis, University of Poitiers (2006).

39. T. Bligaard, J. K. Nørskov. *Electrochim. Acta* **52**, 5512 (2007).
40. Q. Jiang, H. M. Lu, M. Zhao. *J. Phys.: Condens. Matter* **16**, 521 (2004).
41. F. Dassenoy, W. Vogel, N. Alonso-Vante. *J. Phys. Chem. B* **106**, 12152 (2002).
42. P. K. Babu, A. Lewera, J. H. Chung, R. Hunger, W. Jaegermann, N. Alonso-Vante, A. Wieckowski, E. Oldfield. *J. Am. Chem. Soc.* **129**, 15140 (2007).
43. E. R. Savinova, F. Hahn, N. Alonso-Vante. *Phys. Chem. Chem. Phys*. **9**, 5693 (2007).
44. P. K. Babu, E. Oldfiel, A. Wieckowski. "Nanoparticle surfaces studied by electrochemical NMR", in *Modern Aspects of Electrochemistry*, Vol. 36, C. Vayenas, B. E. Conway, R. E. White (Eds.), pp. 1–50, Kluwer Academic/Plenum, New York (2003).
45. J. S. Spendelow, P. K. Babu, A. Wieckowski. *Curr. Opin. Solid State Mater. Sci*. **9**, 37 (2005).
46. J. McBreen, S. Mukerjee. *J. Electrochem. Soc*. **142**, 3399 (1995).
47. G. Samjeske, X.-Y. Xiao, H. Baltruschat. *Langmuir* **18**, 4659 (2002).
48. C. Roth, A. J. Papworth, I. Hussain, R. J. Nichols, D. J. Schiffrin. *J. Electroanal. Chem*. **581**, 79 (2005).
49. M. T. M. Koper. *Surf. Sci*. **548**, 1 (2004).
50. S. Mukerjee, S. Srinivasan, M. P. Soriaga, J. McBreen. *J. Electrochem. Soc*. **142**, 1409 (1995).
51. S. Mukerjee, J. McBreen. *J. Electroanal. Chem*. **448**, 163 (1998).
52. J. F. Drillet, A. Ee, J. Friedemnan, R. Koetz, V. M. Schmidt. *Electrochim. Acta* **47**, 1983 (2002).
53. T. Toda, H. Igarashi, H. Uchida, M. Watanabe. *J. Electrochem. Soc*. **146**, 3750 (1999).
54. U. A. Paulus, A. Wokaun, G. G. Scherer, T. J. Schmidt, N. M. Markovic, P. N. Ross. *J. Phys. Chem. B* **106**, 4181 (2002).
55. N. Alonso-Vante. "Chevrel phase and cluster-like chalcogenide materials", in *Handbook of Fuel Cells*, Vol. 2, W. Vielstich, A. Lamm, H. Gasteiger (Eds.), Part 5, p. 534, John Wiley, Chichester (2003).
56. F. C. Anson, C. Chi, B. Steigert. *Acc. Chem. Res*. **30**, 437 (1997).
57. N. Alonso-Vante. *J. Chim. Phys.* **93**, 702 (1996).
58. R.-F. Wang, S.-J. Liao, H.-Y. Liu, H. Meng. *J. Power Sources* **171**, 471 (2007).